ARTICLE Open Access

# Induced fit growth of Ga-based semiconductor thin films for brain-inspired electronics and optoelectronics

Zixu Sa[1], Kepeng Song[2], You Meng[3], Wenfeng Wu[1], Zhaocong Wang[1], Pengsheng Li[1], Jie Zhang[1], Zeqi Zang[1], Guangcan Wang[1], Mingxu Wang[1], Zhitai Jia[1], Yang Tan[1], Weifeng Li[1]✉, SenPo Yip[4], Feng Chen[1]✉, Johnny C. Ho[3,4,5]✉ and Zai-xing Yang[1]✉

**Abstract**

Current crystalline thin-film production techniques typically require specific growth substrates, posing significant challenges for their use in flexible electronics and integrated optoelectronics. In response to these challenges, we introduce a novel method called 'induced fit growth', inspired by the induced fit theory in molecular biology. This method overcomes the limitations of current techniques by enabling the deposition of Ga-based semiconductor films, including GaSb, GaSe, GaAs, and GaAsSb, with controllable thickness and morphology on arbitrary substrates. Utilizing a low-cost, wafer-scale vapor deposition process compatible with standard semiconductor procedures, these Ga-based films can be patterned for various functional applications. For example, the patterned Ga-based thin films exhibit broad applicability in p-channel transistor arrays (with hole mobility of 0.25 $cm^2 V^{-1} s^{-1}$), functional synaptic devices, and flexible omnidirectional imaging sensors (maintaining functionality at incident angles as low as 5°). Overall, the proposed induced fit growth method facilitates the growth of Ga-based semiconductor films with greater integration flexibility, enhancing their advanced functionality and broad applicability.

## Introduction

Current fabrication methods for semiconductor thin films, which typically rely on post-synthesis assembly and epitaxial growth, face challenges related to processing complexity and high growth temperatures[1–8]. These methods are not fully optimized for the demands of modern Internet of Things (IoT) applications[5,6]. Consequently, existing semiconductor thin films and their production techniques fail to achieve efficient optoelectronic conversion, robust flexibility, transparency, and synaptic behavior required for future multifunctional applications[7–11].

At the same time, among many semiconductor materials, Ga-based thin films, such as $Ga_2O_3$, GaN, GaSe, GaAs, GaSb, and GaAsSb, are known for their high carrier mobilities, tunable bandgaps ranging from ultraviolet to infrared, efficient optical absorption and emission, and adjustable defect and carrier concentrations. These properties are essential in high-speed electronics, broadband photodetection, multicolor light-emitting diodes, and neuromorphic computing[12–19]. Furthermore, functional substrates like flexible mica, transparent glass, ferroelectric oxides, high thermal conductivity substrates, and superconductor substrates enhance the potential of these semiconductor films in wearable optoelectronics, three-dimensional (3D) optical imaging systems, nonvolatile memories, radiofrequency electronics, and spintronics[7,11,20–22]. Therefore, developing feasible growth methods for Ga-based semiconductor films on various

Correspondence: Weifeng Li (lwf@sdu.edu.cn) or
Feng Chen (drfchen@sdu.edu.cn) or Johnny C. Ho (johnnyho@cityu.edu.hk) or
Zai-xing Yang (zaixyang@sdu.edu.cn)
[1]School of Physics, State Key Laboratory of Crystal Materials, Shandong University, Jinan, China
[2]School of Chemistry and Chemical Engineering, Shandong University, Jinan, China
Full list of author information is available at the end of the article
These authors contributed equally: Zixu Sa, Kepeng Song, You Meng, Wenfeng Wu

functional substrates is crucial to facilitate their multifunctionality and scalability.

In general, substrate lattice matching or buffer layers are required to grow semiconductor films[22–26]. However, inspired by induced fit theory in molecular biology, where a substrate induces a conformational change in an enzyme to facilitate binding, we propose an analogous approach for the universal growth of Ga-based semiconductor films on functional substrates[27,28]. Zavabeti et al. demonstrated that an amorphous $GaO_x$ film with residual free Ga atoms could be exfoliated from a liquid Ga surface using a squeeze-printing method[29]. The residual free Ga atoms in the exfoliated amorphous $GaO_x$ film can be considered analogous to the specific enzyme in induced fit theory, promoting the growth of Ga-based semiconductor films.

In this work, we present a novel induced fit growth method for wafer-scale multifunctional Ga-based semiconductor films, such as GaSb, GaSe, GaAs, and GaAsSb, on functional substrates including $Si/SiO_2$, transparent glass, and flexible mica. The thickness and surface roughness of the as-prepared Ga-based semiconductor films can be precisely controlled by adjusting the growth temperature and duration. Furthermore, these films can be patterned into desired shapes, enhancing their utility in flexible electronics and omnidirectional photodetection applications. For instance, GaSb films exhibit typical p-type conductive behavior with a high current density of 0.1 μA $\mu m^{-1}$ and high hole mobility of 0.25 $cm^2 V^{-1} s^{-1}$, along with large-scale uniformity. Enabled by the abundant traps in the interfacial $GaO_x$ film, the patterned GaSb film transistors demonstrate impressive synaptic behaviors. When deposited on transparent glass and flexible mica, the resulting omnidirectional and flexible photodetectors maintain a good photoresponse even at an incident angle of 5° and after 900 folding cycles. These findings highlight a successful strategy for the induced fit growth of multifunctional Ga-based semiconductor films on arbitrary substrates, paving the way for advancements in flexible and multifunctional electronic devices.

## Results

### Induced fit growth of Ga-based semiconductor thin films

Here, the GaSb thin films are prepared using an induced fit growth method, while the experimental details are shown in the "Materials and Methods" section. In short, as shown in Fig. 1a, the $GaO_x$ film is prepared first on

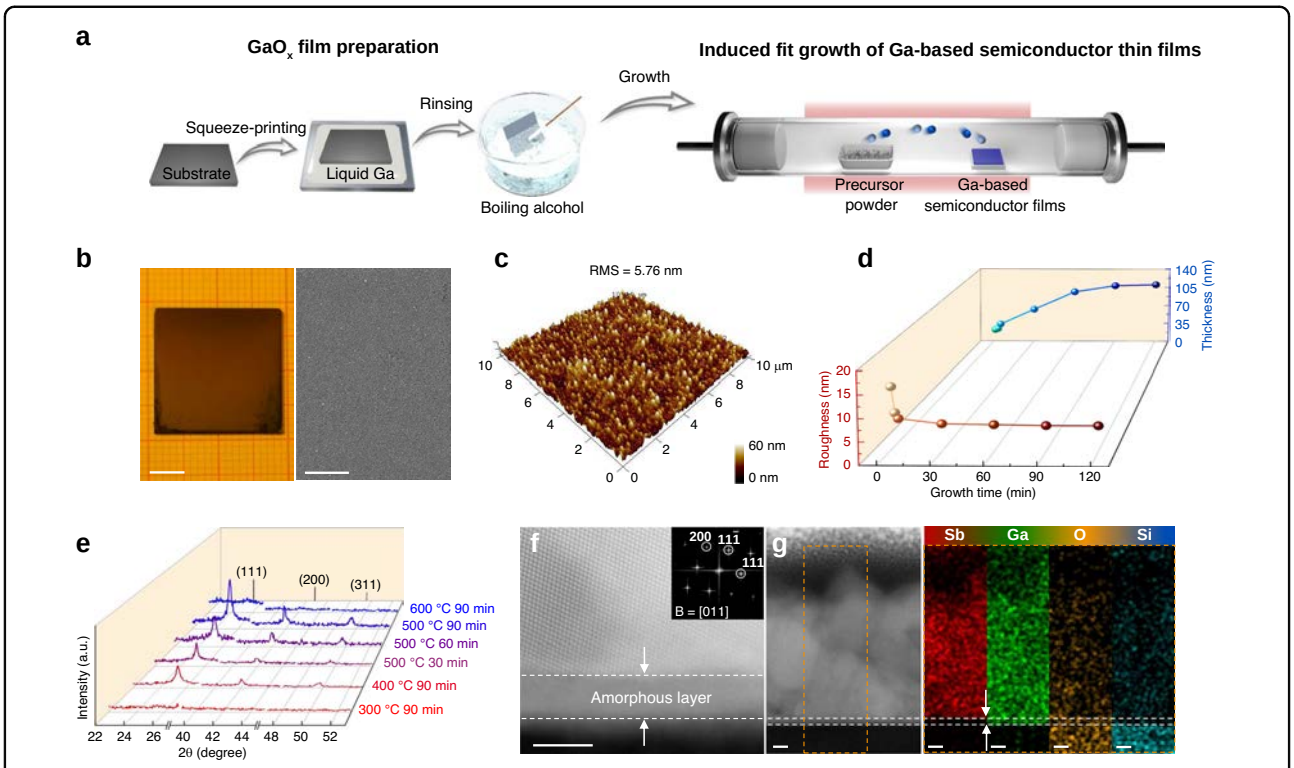


**Fig. 1 Induced fit growth of Ga-based semiconductor thin films. a** Schematic diagrams of the induced fit growth of Ga-based semiconductor films. **b, c** Optical photograph, SEM, and 3D AFM images of the as-prepared GaSb film. The scale bars are 0.5 cm and 5 μm, respectively. **d** Roughness and thickness of the GaSb films prepared with different growth durations. **e** XRD patterns of the GaSb films prepared at different growth temperatures and durations. **f** Cross-sectional HRTEM image of the GaSb film. The inset shows the corresponding FFT pattern. The scale bar is 5 nm. **g**, STEM image and EDS elemental mapping images of Sb, Ga, O, and Si. The scale bars are 10 nm

arbitrary substrates by a reported liquid metal van der Waals exfoliation method[30,31]. As verified by X-ray diffraction (XRD) in Fig. S1, no diffraction peak is observed for the as-exfoliated $GaO_x$ film, demonstrating its amorphous properties. The compact surface and uniform morphology of the as-exfoliated $GaO_x$ thin film are further verified by the atomic force microscope (AFM), as shown in Fig. S2. Then, the as-exfoliated amorphous $GaO_x$ film is utilized to induce fit growth of Ga-based semiconductor thin films in a furnace. Figure 1b, c are the optical photograph, scanning electron microscope (SEM), and 3D AFM images of the as-prepared GaSb film, showing good uniformity of 1.8 cm × 1.8 cm, compact surface morphology, and root mean square (RMS) roughness of 5.76 nm. In fact, the thickness, surface roughness, and crystallinity of GaSb films can be controlled well by growth durations and temperatures. As shown in Fig. 1d, the thickness increases from 22 nm to 108 nm, and the RMS roughness decreases from 14.1 nm to 5.76 nm with the prolongation of growth duration. These values remain almost unchanged after 90 min. The thickness and RMS roughness are deduced from AFM images of Fig. S3. Accordingly, the crystallinity of GaSb films is checked by XRD in Fig. 1e, inferring the as-prepared films to have the zinc blende crystal structure (JCPDS Card No. 07-0215)[32,33]. By optimizing growth temperatures from 300 to 600 °C, more substantial diffraction peaks are observed at 500 °C. No diffraction peaks of GaSb are observed for the growth temperatures of 300 and 600 °C. Meanwhile, the diffraction peaks become stronger when the growth duration extends to 90 min. Scanning transmission electron microscopy (STEM) and energy-dispersive X-ray spectroscopy (EDS) are further adopted to study the crystallinity and stoichiometry of as-prepared GaSb films, as shown in Fig. 1f, g and Fig. S4. As depicted in Fig. 1f, continuous lattice fringes are observed in the cross-sectional GaSb film, and clear reciprocal lattice spots are extracted by fast Fourier transform (FFT), indicating the good crystallinity characteristic. Notably, an obvious amorphous layer with a thickness of 0.37 nm exists between GaSb and the $Si/SiO_2$ substrate. The thickness is in line with the result of AFM in Fig. S2. As displayed in Fig. 1g, the composition of the amorphous layer is Ga and O, and the film is Ga and Sb, illustrating that an amorphous $GaO_x$ film is located between the GaSb film and the $Si/SiO_2$ substrate. Owing to the excellent thermodynamic and chemical stability, the amorphous $GaO_x$ thin film's thickness remains constant during the GaSb thin film's growth process[34,35]. In a word, GaSb films with controlled thickness, surface roughness, and crystallinity can be successfully prepared by the induced fit growth method.

## Growth mechanism of GaSb films by the induced fit growth method

For guiding the growth of multifunctional semiconductor thin films on arbitrary substrates, X-ray photoelectron spectroscopy (XPS) and first-principles calculations are utilized to study the induced fit growth mechanism of GaSb films, as depicted in Fig. 2 and Figs. S5-8. All XPS peaks are calibrated with the C *1 s* peak (284.8 eV) and fitted through Gauss-Lorentz fitting. From the XPS spectra of Ga *3 d* and Sb *4 d* in Fig. S5, the primary/shoulder peaks centered at 20.0/17.9 eV are observed for the as-exfoliated $GaO_x$ film, corresponding to the Ga-O bond and metal Ga, respectively[18]. This indicates that some Ga atoms are completely free in the as-exfoliated $GaO_x$ film[31,36,37]. This result is similar to the film prepared at a low growth temperature of 300 °C. When the growth temperature reaches 400 °C, peaks of the Ga-Sb bond (at 18.5 eV in Ga *3 d* and 31.3/32.6 eV in Sb *4 d*) are observed. However, when the growth temperature reaches 600 °C, only peaks of the Ga-O bond are observed. At the same time, the film prepared at 500 °C shows more substantial Ga-Sb peaks than that prepared at 400 °C. All these results demonstrate the optimal growth temperature of GaSb film as 500 °C, which is in line with the results of XRD in Fig. 1e.

XPS with $Ar^+$ ion etching is further performed to shed light on the growth mechanism, particularly focusing on the interface between the as-exfoliated $GaO_x$ and the as-prepared GaSb film. As shown in Fig. 2a, b, with the prolongation of etching time, the peak intensity of the Ga-O bond first decreases to a constant value and then further reduces to a minimum value. At the same time, the peak intensity of the Ga-Sb bond initially increases, then gradually decreases until it disappears. The peak of the Sb-O bond is only observed in the as-prepared GaSb film. These findings demonstrate that a native oxide layer on the GaSb film surface and a $GaO_x$ film exist at the interface of the GaSb film and the growth substrate. Notably, no peak of metal Ga is observed in Fig. 2a, indicating that it is involved in the growth of GaSb film. To further verify the proposal, the spin-coating $GaO_x$ film is also prepared for the growth of GaSb film, as shown in Figs. S6-S7. As shown in the AFM image, the surface of the spin-coated $GaO_x$ thin film is similar to that of the as-exfoliated $GaO_x$ thin film. However, compared with the as-exfoliated $GaO_x$ film, no peaks of free metal Ga are observed in the XPS of the spin-coating $GaO_x$ film. Using this spin-coating $GaO_x$ film, GaSb film cannot grow at any growth temperature. Obviously, it can be inferred that the free metal Ga in the as-exfoliated $GaO_x$ film facilitates the growth of the GaSb film.

To gain deeper insight into the growth mechanism, simulation computing based on first-principles

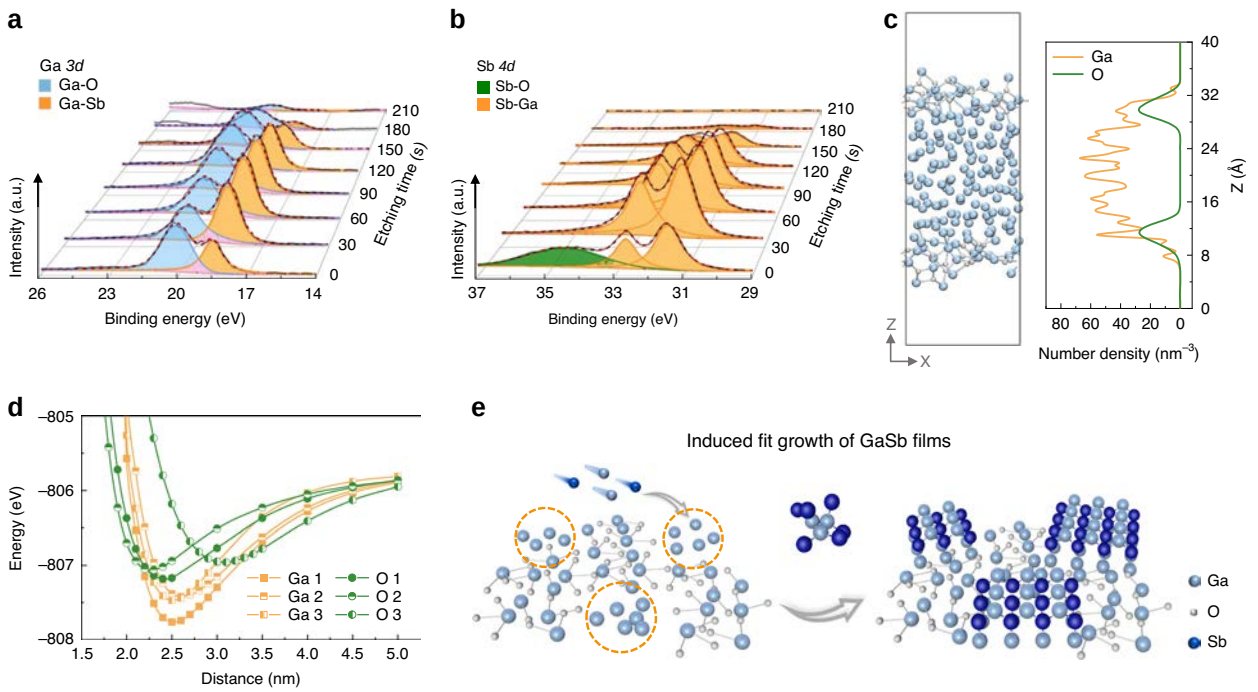


**Fig. 2 Growth mechanism of the induced fit growth method. a, b** XPS spectra of Ga *3 d* and Sb *4 d* of the GaSb films versus etching times. **c** Schematic diagram and the number density distribution of Ga and O atoms along the Z-axis in the optimized $GaO_x$ unit cell. **d** Energy variation curves of the introduced Sb atom as it gradually approaches three selected Ga or O atoms. **e** Schematic diagram of the induced fit growth method for GaSb films

calculations is performed in Fig. 2c, d. As shown in Fig. 2c, the Ga atoms tend to diffuse outward over time, and the O atoms tend to penetrate from the surface into the body, which results in an as-exfoliated Ga-rich $GaO_x$ film. This phenomenon is further verified by the atomic number density profile along the z-axis. Due to free diffusion, some Ga atoms relocate to positions outside the O atoms. Furthermore, as depicted in Fig. 2d and Fig. S8, to explore the thermodynamic behaviors of Sb vapor atoms during the induced fit growth process, the simulations are conducted in which a single Sb atom approaches three randomly selected O atoms or Ga atoms on the surface of the $GaO_x$ film, respectively. The binding energy between Sb and Ga atoms is always lower than that between Sb and O atoms, proving that the introduced Sb atoms bind to Ga atoms more easily than O atoms. The results above reveal that the Ga-rich $GaO_x$ film facilitates the deposition of Sb vapor atoms, thereby promoting the growth of uniform and compact GaSb films. In this case, the schematic diagram of the induced fit growth method for GaSb films is shown in Fig. 2e. The free metal Ga in the as-exfoliated $GaO_x$ film promotes the deposition of Sb vapor, subsequently leading to the island growth of the GaSb film. With the prolonged growth duration, the film gradually becomes compact and uniform. In brief, the as-proposed induced fit growth method paves the way for the growth of multifunctional semiconductor thin films on arbitrary substrates.

## Patterning and electrical properties of GaSb thin films

Microscale patterning is essential but still challenging when using semiconductor thin films for practical applications[38,39]. As shown in Fig. 3, all the induced fit-grown GaSb films can be patterned, and the patterning details can be found in the "Materials and Methods" section. As displayed in the optical images of Fig. 3a, the Chinese zodiac is patterned from the as-prepared GaSb films, exhibiting micrometer-level resolution. The large-scale uniformity is verified by Raman mapping, as presented in Fig. 3b and Fig. S9. With the good patterning ability, the as-prepared GaSb film is then constructed successfully as a transistor array, as illustrated in Fig. 3c, for studying electronic and optoelectronic behaviors. Figure 3d, e show the representative output and transfer characteristics of the as-constructed GaSb thin film transistors, respectively, confirming the ohmic-like contacts between the GaSb films and the Ni electrodes. The output curves versus different $V_{GS}$ for the 90-min-grown GaSb thin film transistor are exhibited in Fig. S10. With the $V_{GS}$ increasing from -20 V to 20 V, the $I_{DS}$ decreases linearly from 7.1 μA to 1.0 μA at the $V_{DS}$ of 1.0 V. The p-type conducting behavior of the as-prepared GaSb films is exhibited. The

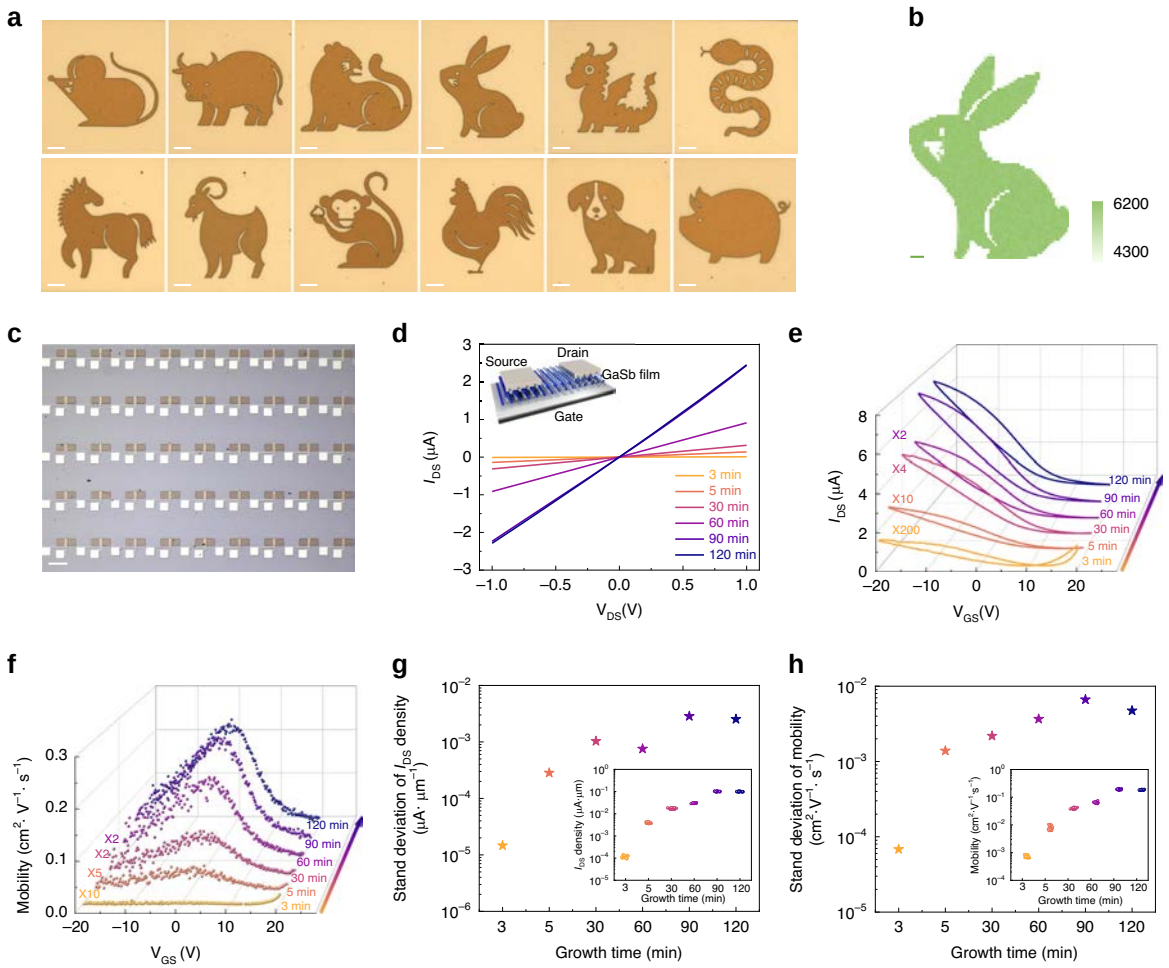


**Fig. 3 Patterning and electrical properties of the as-prepared GaSb thin films. a** Optical images of the Chinese zodiac patterned from the as-prepared GaSb thin films. All scale bars are 50 μm. **b** Raman mapping of a patterned rabbit. The scale bar is 20 μm. **c** Optical image of a patterned transistor array. The scale bar is 200 μm. **d–f** Output, transfer, and mobility characteristics of the as-patterned GaSb films transistors. **g**, **h** Standard variations of $I_{ds}$ density and mobility versus growth duration. The insets are data collected from 20 devices

$I_{DS}$ increases from $0.75 \times 10^{-2}$ to 7.2 μA for the prolonged growth duration. Notably, as depicted in Fig. S11, all the leakage currents are about 100-300 pA, significantly lower than the $I_{DS}$. As displayed in Fig. 3f, the peak hole mobility also increases with the growth duration, reaching a maximum value of 0.25 $cm^2 \cdot V^{-1} \cdot s^{-1}$ at a duration of 90 min. The standard variations of $I_{ds}$ density and mobility are then collected from 20 devices and presented in Fig. 3g, h, further verifying the device performance uniformity of the as-constructed GaSb transistor array. When the growth duration increases from 3 min to 120 min, the standard variation of $I_{DS}$ density increases from $1.5 \times 10^{-5}$ to $2.5 \times 10^{-3}$ μA $\mu m^{-1}$, along with the standard variation of peak hole mobility increasing from $6.8 \times 10^{-5}$ to $4.7 \times 10^{-3}$ $cm^2$ $V^{-1}$ $s^{-1}$. The minor standard deviations of all transistor arrays further verify the uniformity of the as-prepared GaSb films. In short, the induced fit-grown p-type GaSb films are patternable, illustrating their potential as active materials for electronic and optoelectronic devices.

## Synaptic behaviors of GaSb thin films

Realizing that artificial machine intelligence is important for developing neuromorphic computing and the Internet of Things. The synaptic behaviors of the as-constructed 90-minute-grown GaSb thin film transistors are studied in Fig. 4. Figure 4a shows the machine artificial intelligence and biological synapse schematic. As illustrated in Fig. 4b, a postsynaptic current (PSC) can be triggered by a $V_{GS}$ pulse acting on the GaSb film transistor, and the change in PSC is expressed as ΔPSC. PSC decreases when $+V_{GS}$ pulses (width = 100 ms) are applied and quickly reaches peak values when $+V_{GS}$ pulses are removed, then attenuates slowly. These results closely

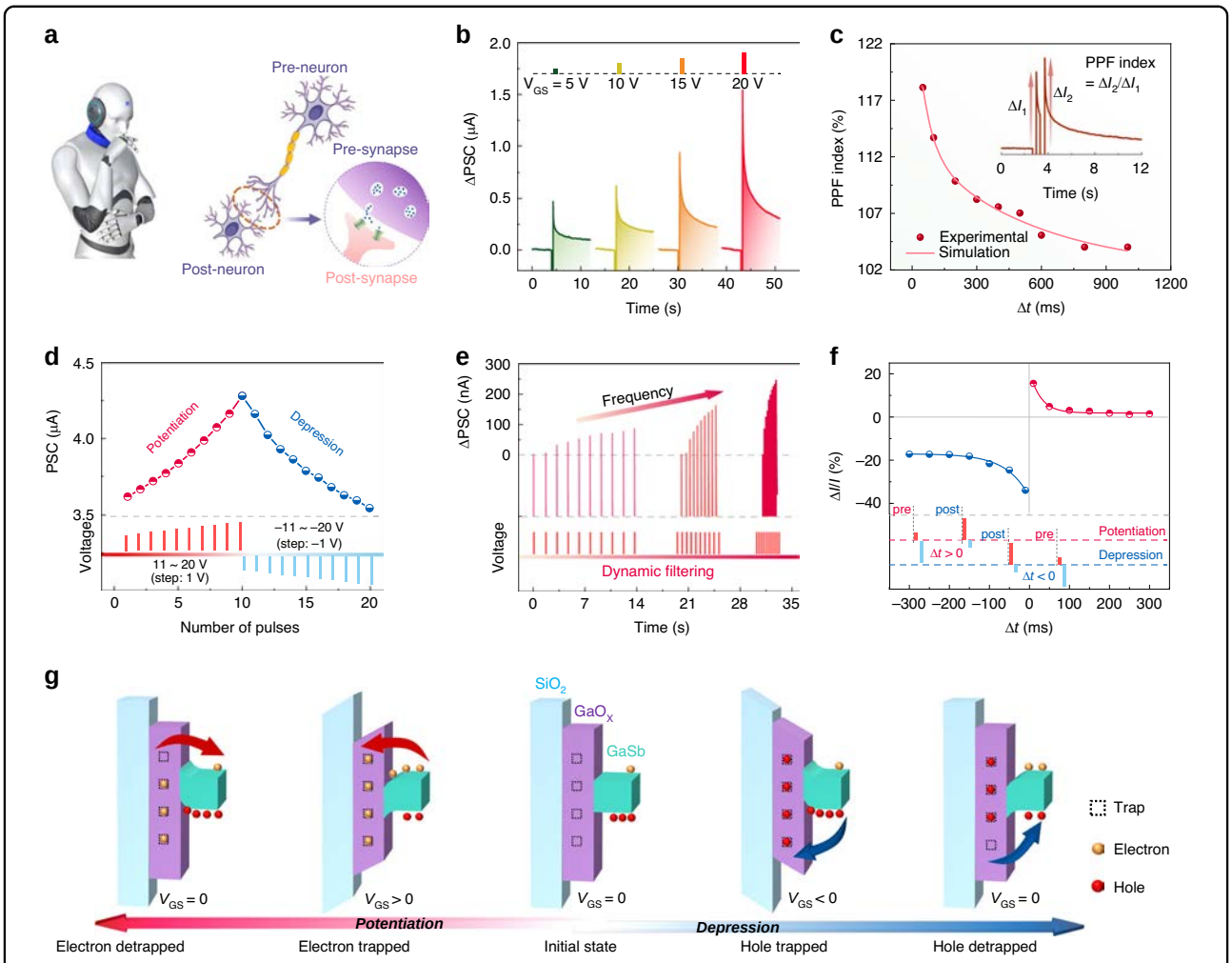


**Fig. 4 Synaptic behaviors of the as-prepared GaSb thin films. a** Schematic diagram of machine artificial intelligence and biological synapse. **b** Synaptic plasticity triggered by positive $V_{GS}$ pulses. **c** PPF index as a function of $V_{GS}$ pulse interval time ($V_{GS}$ = 10 V, width = 100 ms), and the inset is the PSC triggered by a pair of $V_{GS}$ pulses. **d** LTP and LTD realized by continuously applying 20 $V_{GS}$ pulses (width = 100 ms, interval time = 100 ms). **e** SRDP behavior versus different pulse frequencies ($V_{GS}$ = 10 V, width = 100 ms). **f** STDP behavior versus different Δt ($V_{GS}$ = 5/-20 V for pre-stimulation and $V_{GS}$ = 20/-5 V for post-stimulation, width = 100 ms). **g** Proposed charge-trapping model of the as-constructed GaSb film synaptic transistor. All the measurements are under a bias of 1 V

resemble the excitatory PSC (EPSC) process in biological synapses[40,41]. The $V_{GS}$ pulses increase from 5 to 20 V, and the ΔPSC increases from 0.47 to 1.5 μA, inferring the successful transition of short-term plasticity (STP) to long-term plasticity (LTP). The inverse synaptic behavior is observed in Fig. S12. When -$V_{GS}$ pulses are applied and removed, exhibiting programmable depression behaviors. Moreover, as shown in Fig. S13, all the as-prepared GaSb thin film synaptic transistors exhibit $V_{GS}$-dependent synaptic behaviors with uniform responses to identical external $V_{GS}$ stimulations, verifying the robust reliability and uniformity. As a typical biological synaptic behavior, paired pulse facilitation (PPF), a phenomenon where synaptic weight stimulated by the second spike increases when it closely follows the first, plays a vital role in decoding temporal information in auditory or visual signals. As depicted in the inset of Fig. 4c, the PSC triggered by the second $V_{GS}$ pulse ($\Delta I_2$) is larger than that triggered by the first pulse ($\Delta I_1$), a typical PPF behavior characteristic[41]. The PPF is described using the following equation: $PPF = 1 + C_1\exp(\Delta t/\tau_1) + C_2\exp(\Delta t/\tau_2)$, in which $C_1$ and $C_2$ are the initial facilitation magnitudes of rapid and slow phases, $\tau_1$ and $\tau_2$ are the characteristic relaxation times of the rapid and slow decay, respectively, and Δt is the pulse interval. The values of $\tau_1$ (53.5 ms) and $\tau_2$ (541.3 ms) are exhibited. The PPF index, defined as $\Delta I_2/\Delta I_1$, can reach up to 118% when Δt is 50 ms. It decreases exponentially as the Δt increases. The LTP and long-term depression (LTD) are also successfully mimicked via a series of electrical stimulations in Fig. 4d, exhibiting good linearity

and symmetry. Next, the Hebbian learning rule is mimicked by the GaSb thin film transistor, including spike rate-dependent plasticity (SRDP) and spike timing-dependent plasticity (STDP). As shown in Fig. 4e, ΔPSC increases with the $V_{GS}$ frequency, and the dynamic filtering is realized, demonstrating SRDT behavior. On the other hand, STDP characterizes the synaptic weight change resulting from the temporal interval. As depicted in Fig. 4f, the arrival orders of pre- and post-stimulations determine potentiation or depression, indicating that the synapse shows potentiation/depression when Δt is positive/negative. In a word, various typical synaptic behaviors, including STP, LTP, PPF, SRDP, and STDP, are successfully mimicked by the GaSb thin film transistors.

Notably, to validate the mechanism that enables synaptic behaviors, the top-gated GaSb thin film transistor is constructed and studied in Fig. S14. Compared with the back-gated transistor, there is no amorphous $GaO_x$ film between the dielectric and the GaSb film in the as-constructed top-gated transistor. When the positive or negative $V_{GS}$ pulses are applied, no obvious synaptic behaviors are observed. Based on the above results, a charge-trapping model is proposed to explain the synaptic behaviors of the as-prepared GaSb thin film transistor, in which the amorphous $GaO_x$ film serves as the charge trap layer to capture carriers, as depicted in Fig. 4g. The middle picture represents the initial state. When a $+V_{GS}$ ($-V_{GS}$) pulse is applied to the back gate, electrons (holes) are driven to the amorphous $GaO_x$ film and trapped there. Once the $+V_{GS}$ ($-V_{GS}$) pulse is removed, the trapped electrons (holes) turn the GaSb channel to an on-state (off-state), representing the potentiation (depression). As time passes, the trapped electrons (holes) would be released, leading to decreased (increased) hole carriers in the GaSb channel. Therefore, benefiting from the use of amorphous $GaO_x$ film during the induced fit growth process, the as-prepared GaSb thin films are promising for developing neuromorphic computing.

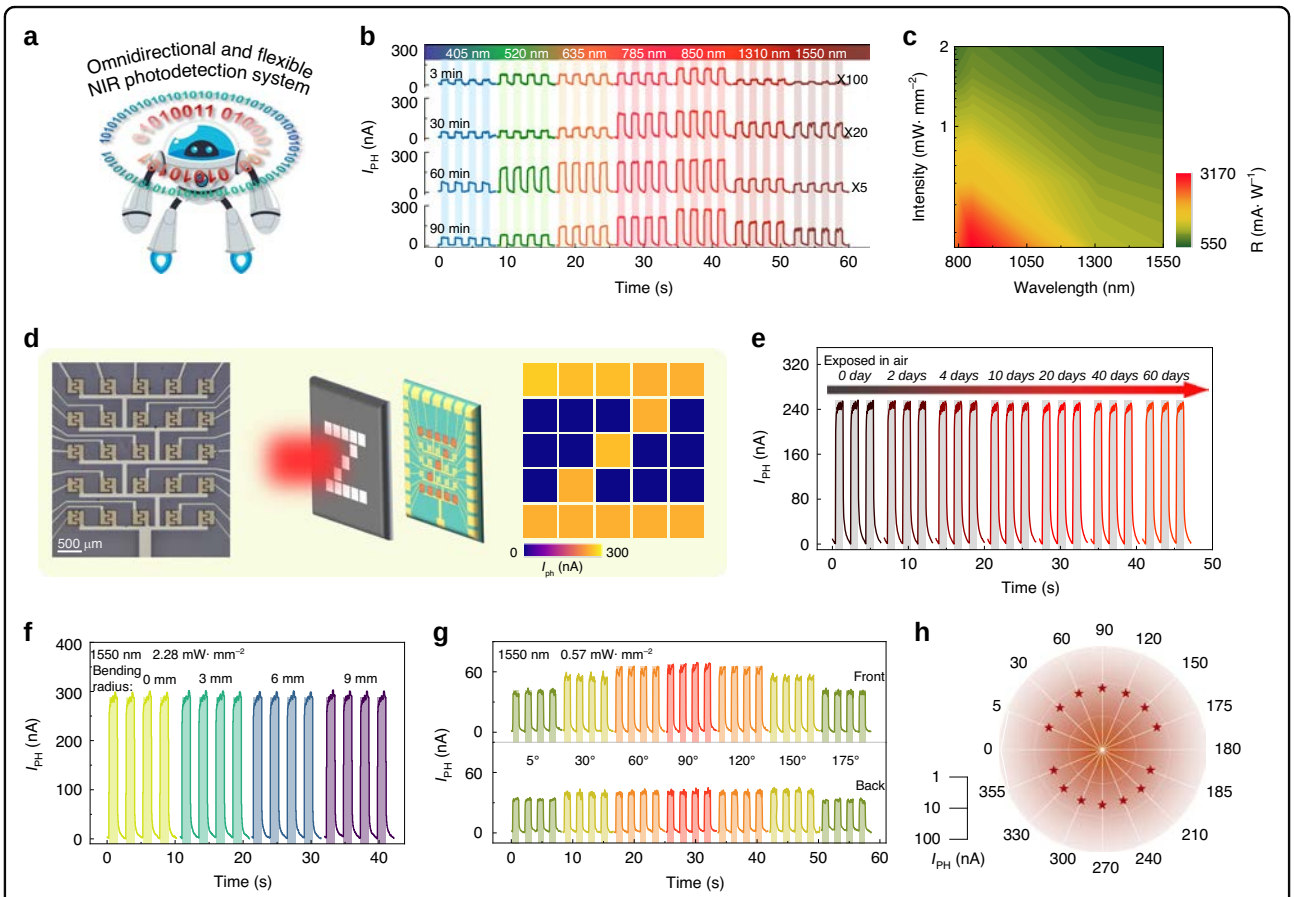


**Fig. 5 Photodetection behaviors of the as-prepared GaSb thin films. a** Schematic diagram of the omnidirectional and flexible NIR photodetection system. **b** Wavelength-dependent broadband photodetection behaviors of the as-prepared GaSb films. The laser intensity is 0.57 mW·mm$^{-2}$. **c** Two-dimensional contour map of R versus different wavelengths and laser intensities. **d** Demonstration of the NIR photodetection imaging system. **e** Air stability of the as-studied NIR photodetector. **f** Time-resolved photoresponse of the as-fabricated flexible NIR photodetector after different bending radii. **g**, **h** Omnidirectional photodetection behaviors of the as-fabricated NIR photodetector. All the measurements are under a bias of 1 V

### Photodetection behaviors of GaSb thin films

Flexibility and transparency are critical requirements for the omnidirectional and flexible NIR photodetection system, as shown in Fig. 5a. In this regard, the photodetection performance of the as-fabricated GaSb thin film transistors is investigated and presented in Fig. 5b–e. As expected, all the as-fabricated photodetectors exhibit broadband photodetection behaviors, owing to the narrow bandgap of GaSb (0.72 eV), as depicted in Fig. 5b and Figs. S15-S16. With the increasing thin film growth duration, the photocurrent ($I_{PH} = I_{light} - I_{dark}$) increases from 8 to 274 nA under the illumination of an 850 nm laser with an intensity of 0.57 $mW{\cdot}mm^{-2}$. This phenomenon may result from the increased thickness of the thin films. At the same time, the $I_{PH}$ can be effectively modulated by periodic laser illumination, demonstrating reproducible dynamic stability. Another two critical parameters of photodetectors, responsivity (R) and detectivity (D*) of the GaSb film grown by 90 min, are studied in Fig. 5c and Fig. S17. Generally speaking, R can be defined as $R = I_{PH}/(PA)$, and D* can be defined as $D^* = RA^{1/2}/(2eI_{dark})^{1/2}$, in which P is the incident power density, A is the effective irradiated area, e is the electronic charge, and $I_{dark}$ is dark current[42,43]. As a result, the maximum R and D* can be as high as 3170 $mA{\cdot}W^{-1}$ and $5.3 \times 10^9$ Jones under the illumination of an 850 nm laser with an intensity of 0.28 $mW\ mm^{-2}$. As shown in Fig. S18, the response time, including rise time ($\tau_r$) and decay time ($\tau_d$), is defined as the time for the photocurrent to increase/decrease from 10/90% to 90/10%[44,45]. Obviously, the as-constructed photodetector exhibits $\tau_r$ of 11 ms and $\tau_d$ of 18 ms, respectively, comparable with the photodetectors based on other semiconductor thin films[46,47]. Because of the excellent NIR photodetector performance, a 5 × 5-pixel NIR imaging array is constructed by the as-prepared GaSb thin film, as illustrated in Fig. 5d. A hollow target mask of the letter "Z" is placed before the photodetector array. The precise and uniform imaging results demonstrate the excellent NIR photoresponse and uniformity of the as-prepared GaSb thin film. Then, the air stability of the as-prepared GaSb thin film photodetector is also evaluated and compiled in Fig. 5e. No apparent attenuation of $I_{PH}$ is observed after exposure to ambient for 60 days, designating excellent air stability and robust operation of the as-prepared GaSb thin film photodetector.

Benefiting from the weak substrate dependence of the induced fit growth method, GaSb thin films can be readily prepared on various functional substrates, such as flexible mica and rigid glass. Correspondingly, flexible and omnidirectional NIR photodetectors can be fabricated and examined. All fabricated photodetectors exhibit ohmic contact. By adopting the flexible and transparent growth substrate of mica, the photoresponse of the as-prepared GaSb thin film maintains even after 900 bending-recovering cycles and bending at a radius of 3 mm under the illumination of a 1550 nm laser, exhibiting good bendability and flexibility, as shown in Fig. 5f and Fig. S19. When the laser irradiates the photodetector in omnidirectional directions, the variation of $I_{PH}$ is recorded and shown in Fig. 5g, h. Notably, a stable photoresponse can be observed at an incident angle of 5°. The $I_{PH}$ can keep over 64% compared to that at an incident angle of 90°, indicating excellent omnidirectional photodetection performance. This excellent omnidirectional photodetection performance can also be observed when rigid glass is used as the growth substrate, as shown in Fig. S20. As a result, due to the induced fit growth process, the as-prepared GaSb thin films are promising as active channels for omnidirectional and flexible NIR photodetection systems for wearable devices.

### Versatility of the induced fit growth method

Owing to the free metal Ga on the as-exfoliated $GaO_x$ film, the induced fit growth method can also be demonstrated as a successful growth approach for other Ga-based semiconductor thin films, such as GaSe, GaAs, and GaAsSb, as shown in Fig. 6. Figure 6a and Fig. S21 illustrate the AFM images of the films, and the thicknesses of the GaSe, GaAs, and GaAsSb films are 204 nm, 92 nm, and 173 nm, along with the RMS roughnesses of 19.1 nm, 10.8 nm, and 9.21 nm, respectively. All these films display a compact surface morphology. The XRD patterns and Raman spectra in Fig. S22 confirm their good crystallinity and uniform composition. As shown in Fig. S23, the as-prepared GaAsSb, GaAs, and GaSe thin films exhibit p-type, n-type, and p-type conducting behaviors, respectively. Similar to the GaSb counterpart, the GaAsSb thin film transistor also displays fantastic synaptic behaviors in Fig. 6b, c and Fig. S24 due to the charge-trapping role of $GaO_x$ film at the interface of GaAsSb film and growth substrate. As the $V_{GS}$ pulses increase from 5 to 20 V, the successful transition of STP to LTP is observed in Fig. 6b. As shown in Fig. 6c, the PPF index of the GaAsSb film synaptic transistor can reach up to 125% when Δt is 50 ms. Furthermore, the photodetection behaviors of the as-prepared Ga-based semiconductors are also studied in Fig. 6d–f and Fig. S25. With the bandgaps covered from UV to NIR, all these Ga-based semiconductors show excellent broadband photoresponse. The $I_{PH}$ can be effectively modulated by periodic laser illumination, demonstrating reproducible dynamic stability. The maximal R values of GaSe, GaAs, and GaAsSb films are 940 $mA{\cdot}W^{-1}$, along with the maximal D* values of $5.7 \times 10^9$ Jones. At the same time, the corresponding $\tau_r/\tau_d$ values of GaSe, GaAs, and GaAsSb films are 8/12, 6/8, and 12/26 ms, respectively. The induced fit growth method paves an efficient way to the controllable growth of multifunctional Ga-based semiconductor thin films.

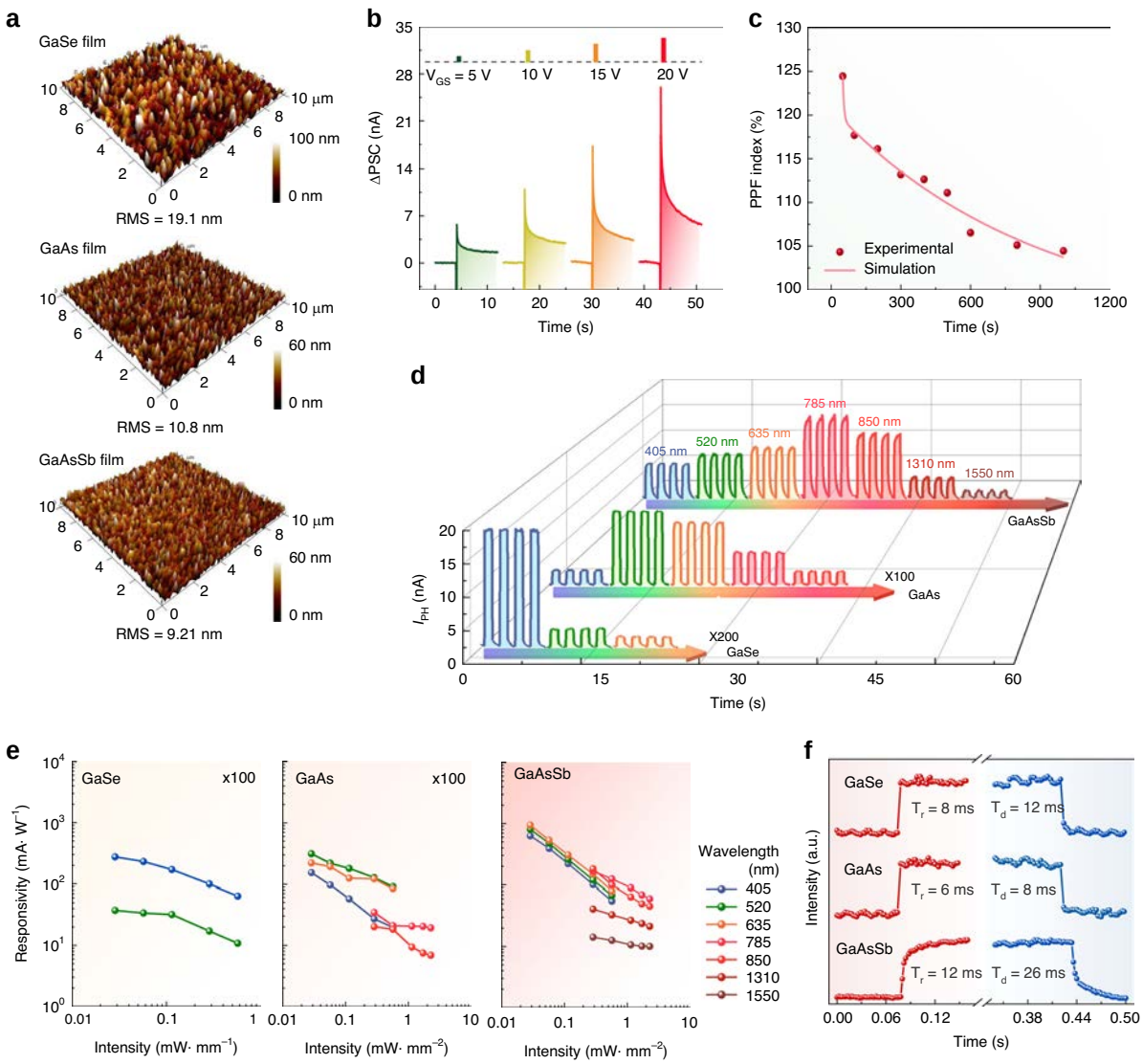


**Fig. 6 Versatility of the induced fit growth method for multifunctional Ga-based semiconductor thin films. a** 3D AFM images of the as-prepared GaSe, GaAs, and GaAsSb thin films. **b, c** Synaptic plasticity and PPF behaviors of the GaAsSb thin film transistor. **d** Wavelength-dependent broadband photodetection behaviors of the as-prepared GaSe, GaAs, and GaAsSb thin films. The laser intensity is 0.57 mW·mm$^{-2}$. **e, f** Wavelength-dependent R and temporal photoresponse of GaSe, GaAs, and GaAsSb thin films. All the measurements are under a bias of 1 V

## Discussion

Recently, many growth technologies, such as interfacial epitaxy methodology, surface chemistry of growth substrates, and modularized growth strategy, have been developed for the wafer-scale growth of Van der Waals semiconductors, such as the transition-metal dichalcogenides[48–53]. In this work, we have successfully prepared large-scale multifunctional Ga-based semiconductor thin films, including GaSb, GaSe, GaAs, and GaAsSb, on various substrates using an induced fit growth method. The thickness and surface roughness of these films can be effectively controlled by adjusting the growth temperature and duration. Notably, the GaSb films exhibit easy patterning capabilities and have been utilized to construct transistors, which display typical p-type conductive behaviors and synaptic functions. Additionally, when GaSb films are prepared on transparent glass and flexible mica, the resulting omnidirectional and flexible photodetectors maintain excellent photoresponse even at an incident angle of 5° and after 900 folding cycles. These results highlight the efficacy of the induced fit growth strategy for Ga-based semiconductor thin films. Furthermore, the growth and photoelectronic properties of other Ga-based semiconductor films, such as GaSe, GaAs, and GaAsSb, have also been successfully demonstrated. These findings underscore a straightforward and effective

strategy for the induced fit growth of multifunctional semiconductor thin films.

It is worth pointing out that GaSb has been considered a promising thermoelectric material, owing to its high Seebeck coefficient and good electrical conductivity[54]. However, the relatively high thermal conductivity limits its thermoelectric figure of merit, ZT[55]. To improve the thermoelectric performance, further works can focus on doping or nanostructuring large-scale GaSb thin films using this induced fit growth method[55,56]. With high optical absorption and a direct bandgap, GaAs provides advantages in solar cells[57]. Moreover, GaAs is resistant to heat and radiation damage due to the higher threshold energy under high-energy radiation, promising for radiation-resistant devices[58]. In the case of GaSe, it shows room-temperature ferroelectricity, benefiting from the unique intralayer sliding and atomic vacancy defect, which promises nonvolatile memory and optoelectronic devices[59,60]. In short, the as-studied Ga-based semiconductor thin films grown by the induced fit growth method also significantly promise the future high-performance thermoelectric devices, solar cells, ferroelectric memory, etc.

## Materials and Methods

### Induced fit growth of Ga-based semiconductor films

Ga-based semiconductor films are prepared by a proposed induced fit growth method in a dual-zone horizontal tube furnace. The liquid metal van der Waals exfoliation method is used to prepare the $GaO_x$ film. The metal Ga remains liquid when placed on glass under heating. The substrate is gently squeezed vertically onto the surface of the droplet. When the substrate is lifted, the continuous and uniform $GaO_x$ film is transferred onto the surface of the substrate. The visible residual liquid Ga droplets are removed by rinsing with boiling alcohol. Next, the high-purity Ga-based semiconductor powders (99.999% purity) are placed in the upstream zone, while the growth substrates with $GaO_x$ films are placed in the downstream zone. The upstream zone is heated to 750, 850, 800, and 770 °C, while the downstream zone is heated to 500, 400, 550, and 500 °C for the growth of GaSb, GaSe, GaAs, and GaAsSb films, respectively. The heating rate is set to 10 °C/min. The system is pumped to $7\times10^{-3}$ Torr. Upstream precursor steam is transported by nitrogen (99.999% purity, 50 sccm) to the downstream zone. When it reaches the set time, the upstream and downstream zones stop together and cool to room temperature under the nitrogen flow.

### Material characterizations

The morphologies are characterized using a microscope (Olympus microscope BX53M) and SEM (Helios G4 UC, Thermo Scientific). The morphologies and heights of the as-prepared films are characterized by AFM (Dimension Icon). The crystal phase and phase purity of the as-prepared films are verified by XRD (D8 Advance, Bruker). The microstructure and composition characterizations are characterized by TEM and HRTEM associated with EDS mapping (Spectra 300, Thermofisher). The chemical composition and elemental valence are analyzed by XPS (Nexsa, Thermo Scientific). Raman (Nanobase XperRAM) spectra and mappings are obtained with 532 nm excitation wavelengths.

### Film etching

The negative photoresist or Polymethyl Methacrylate (PMMA) is spin-coated on the sample surface, and then standard photolithography or electron beam lithography is adopted. After the developing process, a tetramethylammonium hybrid solution is used for film etching. Then, 1-Methyl-2-pyrrolidinone or acetone removes the residue photoresist or PMMA.

### Device fabrication and measurements

A copper grid is placed on the top of the as-prepared films as a shadow mask for resist-free metal evaporation. A 50 nm thick Ni film is deposited as contact metal via e-beam evaporation. A SourceMeter (Keithley 2602B) is used to assess the electrical performance in response to applied electrical pulses. In an atmospheric environment, electrical and photodetection performance is characterized by a standard electrical probe station and a semiconductor analyzer (Agilent B1500A). A semiconductor analyzer is the current signal acquisition equipment, and diode lasers are the light source. The laser intensity is calibrated by a power meter.

### Simulation calculation

The first-principles calculations are carried out using the density functional theory in the Vienna Ab initio Simulation Package using the plane-wave pseudopotential method[61]. The generalized gradient approximation in the form of Perdew–Burke–Ernzerhof is used to describe the exchange-correlation of electrons[62]. The energy cutoff of the plane wave is set as 500 eV, and the energy and force convergence thresholds are set to be $10^{-6}$ eV and $10^{-2}$ eV/Å, respectively. The Grimme method (DFT-D3) is used to correct the weak Van der Waals interaction[63]. The $GaO_x$ unit cell is obtained by expanding the Ga elemental cell and substituting the Ga atoms in both the top and bottom two atomic layers with O atoms in a 1:1 ratio. The molecular dynamics simulations are performed for 50,000 steps with a 1 fs time step. A Nosé thermostat maintains the system temperature at 350 K throughout the simulation[64]. The Brillouin zone is sampled with a k-point mesh of $1 \times 1 \times 1$ for the rectangular unit cell of $GaO_x$.

**Acknowledgements**
We acknowledge the National Natural Science Foundation of China (No. 61904096), Natural Science Foundation of Shandong Province (Nos. ZR2022JQ05 and ZR2024MF010), and a fellowship award from the Research Grants Council of the Hong Kong Special Administrative Region, China (CityU RFS2021-1S04).

**Author details**
[1]School of Physics, State Key Laboratory of Crystal Materials, Shandong University, Jinan, China. [2]School of Chemistry and Chemical Engineering, Shandong University, Jinan, China. [3]Department of Materials Science and Engineering, City University of Hong Kong, Hong Kong, China. [4]Institute for Materials Chemistry and Engineering, Kyushu University, Fukuoka, Japan. [5]State Key Laboratory of Terahertz and Millimeter Waves, City University of Hong Kong, Hong Kong, China

**Author contributions**
Z.Y. conceived the project. Z.Y., Z.S., W.L., F.C., and J.H. designed the experiments and wrote the manuscript. Z.S. and J.Z. contributed to the growth of Ga-based semiconductor films and AFM measurement. K.S. performed HRTEM and STEM. W.W. and W.L. contributed to the simulation calculations. Z.W. contributed to the Raman measurement. P.L. and Z.Z. contributed to the SEM and XRD measurements. G.W. and M.W. contributed to the XPS measurement. Z.S. contributed to the device performance measurement. Y.M., Z.J., Y.T., and S.Y. provided useful discussions. All authors have discussed the results and commented on the manuscript.

**Data availability**
All data that support the findings of this work are available within the paper. Additional data are available from the corresponding authors upon request.

**Conflict of interest**
The authors declare no conflict of interests.

**Supplementary information** The online version contains supplementary material available at https://doi.org/10.1038/s41377-025-02096-2.

Received: 19 May 2025 Revised: 16 September 2025 Accepted: 11 October 2025
Published online: 04 February 2026

**References**

1. Kim, K. S. et al. Non-epitaxial single-crystal 2D material growth by geometric confinement. *Nature* **614**, 88–94 (2023).
2. Liu, C. et al. Understanding epitaxial growth of two-dimensional materials and their homostructures. *Nat. Nanotechnol.* **19**, 907–918 (2024).
3. Wang, J. M. et al. Group-III nitride heteroepitaxial films approaching bulk-class quality. *Nat. Mater.* **22**, 853–859 (2023).
4. Li, T. T. et al. Epitaxial growth of wafer-scale molybdenum disulfide semiconductor single crystals on sapphire. *Nat. Nanotechnol.* **16**, 1201–1207 (2021).
5. Zhang, X. Q. et al. Epitaxial growth of large-scale 2D $CrTe_2$ films on amorphous silicon wafers with low thermal budget. *Adv. Mater.* **36**, 2311591 (2024).
6. Haggren, T., Tan, H. H. & Jagadish, C. III–V thin films for flexible, cost-effective, and emerging applications in optoelectronics and photonics. *Acc. Mater. Res.* **4**, 1046–1056 (2023).
7. Lien, M. B. et al. Ranging and light field imaging with transparent photodetectors. *Nat. Photonics* **14**, 143–148 (2020).
8. Morteza Najarian, A. et al. Photophysical properties of materials for high-speed photodetection. *Nat. Rev. Phys.* **6**, 219–230 (2024).
9. Du, B. C. et al. A water-resistant, ultrathin, conformable organic photodetector for vital sign monitoring. *Sci. Adv.* **10**, eadp2679 (2024).
10. Shim, H. et al. An elastic and reconfigurable synaptic transistor based on a stretchable bilayer semiconductor. *Nat. Electron.* **5**, 660–671 (2022).
11. Li, Q. T. et al. Transparent multispectral photodetectors mimicking the human visual system. *Nat. Commun.* **10**, 4982 (2019).
12. Zhang, Z. F. et al. In-sensor reservoir computing system for latent fingerprint recognition with deep ultraviolet photo-synapses and memristor array. *Nat. Commun.* **13**, 6590 (2022).
13. Memon, M. H. et al. A three-terminal light emitting and detecting diode. *Nat. Electron.* **7**, 279–287 (2024).
14. Jia, H. Q. et al. Recent progress in GaN-based light-emitting diodes. *Adv. Mater.* **21**, 4641–4646 (2009).
15. Late, D. J. et al. GaS and GaSe ultrathin layer transistors. *Adv. Mater.* **24**, 3549–3554 (2012).
16. Wang, P. et al. Arrayed van der Waals broadband detectors for dual-band detection. *Adv. Mater.* **29**, 1604439 (2017).
17. Convertino, C. et al. A hybrid III–V tunnel FET and MOSFET technology platform integrated on silicon. *Nat. Electron.* **4**, 162–170 (2021).
18. Li, J. et al. Template approach to large-area non-layered Ga-group two-dimensional crystals from printed skin of liquid Gallium. *Chem. Mater.* **33**, 4568–4577 (2021).
19. Schulte, K. L. et al. GaAs solar cells grown on acoustically spalled GaAs substrates with 27% efficiency. *Joule* **7**, 1529–1542 (2023).
20. Kang, S. et al. Highly enhanced ferroelectricity in $HfO_2$-based ferroelectric thin film by light ion bombardment. *Science* **376**, 731–738 (2022).
21. Kang, J. S. et al. Integration of boron arsenide cooling substrates into gallium nitride devices. *Nat. Electron.* **4**, 416–423 (2021).
22. Yan, R. S. et al. GaN/NbN epitaxial semiconductor/superconductor heterostructures. *Nature* **555**, 183–189 (2018).
23. Manzo, S. et al. Pinhole-seeded lateral epitaxy and exfoliation of GaSb films on graphene-terminated surfaces. *Nat. Commun.* **13**, 4014 (2022).
24. Zhao, T. G. et al. Substrate engineering for wafer-scale two-dimensional material growth: strategies, mechanisms, and perspectives. *Chem. Soc. Rev.* **52**, 1650–1671 (2023).
25. Wang, J. H. et al. Dual-coupling-guided epitaxial growth of wafer-scale single-crystal $WS_2$ monolayer on vicinal *a*-plane sapphire. *Nat. Nanotechnol.* **17**, 33–38 (2022).
26. Chen, Y. X. et al. Universal growth of ultra-thin III–V semiconductor single crystals. *Nat. Commun.* **11**, 3979 (2020).
27. Koshland, D. E. The key–lock theory and the induced fit theory. *Angew. Chem. Int. Ed. Engl.* **33**, 2375–2378 (1995).
28. Neubig, R. R. & Thomsen, W. J. How does a key fit a flexible lock? Structure and dynamics in receptor function. *BioEssays* **11**, 136–141 (1989).
29. Zavabeti, A. et al. A liquid metal reaction environment for the room-temperature synthesis of atomically thin metal oxides. *Science* **358**, 332–335 (2017).
30. Castilla-Amorós, L. et al. Modulating the reactivity of liquid Ga nanoparticle inks by modifying their surface chemistry. *J. Am. Chem. Soc.* **144**, 1993–2001 (2022).
31. Kochat, V. et al. Atomically thin gallium layers from solid-melt exfoliation. *Sci. Adv.* **4**, e1701373 (2018).
32. Liu, F. J. et al. Lattice-mismatch-free construction of III-V/chalcogenide core-shell heterostructure nanowires. *Nat. Commun.* **14**, 7480 (2023).
33. Sa, Z. et al. Toward high bias-stress stability p-type GaSb nanowire field-effect-transistor for gate-controlled near-infrared photodetection and photocommunication. *Adv. Funct. Mater.* **33**, 2304064 (2023).
34. Hou, X. H. et al. High-performance harsh-environment-resistant $GaO_x$ solar-blind photodetectors via defect and doping engineering. *Adv. Mater.* **34**, 2106923 (2022).
35. Shi, Y. H. et al. High-performance a-ITZO TFTs with high bias stability enabled by self-aligned passivation using a-$GaO_x$. *Appl. Phys. Lett.* **121**, 212101 (2022).
36. Syed, N. et al. Wafer-sized ultrathin Gallium and Indium Nitride nanosheets through the ammonolysis of liquid metal derived oxides. *J. Am. Chem. Soc.* **141**, 104–108 (2019).
37. Carey, B. J. et al. Wafer-scale two-dimensional semiconductors from printed oxide skin of liquid metals. *Nat. Commun.* **8**, 14482 (2017).
38. Meng, Y. et al. An inorganic-blended p-type semiconductor with robust electrical and mechanical properties. *Nat. Commun.* **15**, 4440 (2024).
39. Meng, Y. et al. Van der Waals nanomesh electronics on arbitrary surfaces. *Nat. Commun.* **14**, 2431 (2023).
40. Wang, S. Y. et al. A $MoS_2$/PTCDA hybrid heterojunction synapse with efficient photoelectric dual modulation and versatility. *Adv. Mater.* **31**, 1806227 (2019).
41. Dang, Z. Y. et al. Black phosphorus/ferroelectric P(VDF-TrFE) field-effect transistors with high mobility for energy-efficient artificial synapse in high-accuracy neuromorphic computing. *Nano Lett.* **23**, 6752–6759 (2023).
42. Xu, T. F. et al. Van der Waals mid-wavelength infrared detector linear array for room temperature passive imaging. *Sci. Adv.* **10**, eadn0560 (2024).

43. Wang, F. et al. How to characterize figures of merit of two-dimensional photodetectors. *Nat. Commun.* **14**, 2224 (2023).
44. Wang, H. Y. et al. Approaching the external quantum efficiency limit in 2D photovoltaic devices. *Adv. Mater.* **34**, 2206122 (2022).
45. Zhong, M. Z. et al. Gate controllable band alignment transition in 2D black-arsenic/$WSe_2$ heterostructure. *Appl. Phys. Rev.* **10**, 021416 (2023).
46. Teng, F. et al. Photoelectric detectors based on inorganic p-type semiconductor materials. *Adv. Mater.* **30**, 1706262 (2018).
47. Wu, W. Q. et al. Flexible photodetector arrays based on patterned $CH_3NH_3PbI_{3-x}Cl_x$ perovskite film for real-time photosensing and imaging. *Adv. Mater.* **31**, 1805913 (2019).
48. Qin, B. et al. Interfacial Epitaxy of multilayer rhombohedral transition-metal dichalcogenide single crystals. *Science* **385**, 99–104 (2024).
49. Zhu, H. Y. et al. Step engineering for nucleation and domain orientation control in $WSe_2$ epitaxy on *c*-plane sapphire. *Nat. Nanotechnol.* **18**, 1295–1302 (2023).
50. Xue, G. D. et al. Modularized batch production of 12-inch transition metal dichalcogenides by local element supply. *Sci. Bull.* **68**, 1514–1521 (2023).
51. Liu, L. et al. Uniform nucleation and epitaxy of bilayer molybdenum disulfide on sapphire. *Nature* **605**, 69–75 (2022).
52. Liu, L. et al. Homoepitaxial growth of large-area rhombohedral-stacked $MoS_2$. *Nat. Mater.* **24**, 1195–1202, https://doi.org/10.1038/s41563-025-02274-y (2025).
53. Wu, D. et al. Phase-controlled van der Waals growth of wafer-scale 2D $MoTe_2$ layers for integrated high-sensitivity broadband infrared photodetection. *Light Sci. Appl.* **12**, 5 (2023).
54. Patapis, S. K. Two thermomagnetic effects and the electronic thermal conductivity in p-GaSb. *Solid State Commun.* **46**, 527–529 (1983).
55. Yan, Y. C. et al. Achieving high power factor in GaSb with intrinsically high mobility via Ge doping. *Rare Met.* **43**, 5435–5441 (2024).
56. Kim, C. E. et al. Thermoelectric properties of Zn-doped GaSb. *J. Appl. Phys.* **111**, 043704 (2012).
57. Yoon, J. et al. GaAs photovoltaics and optoelectronics using releasable multilayer epitaxial assemblies. *Nature* **465**, 329–333 (2010).
58. Polman, A. et al. Photovoltaic materials: present efficiencies and future challenges. *Science* **352**, aad4424 (2016).
59. Li, W. H. et al. Emergence of ferroelectricity in a nonferroelectric monolayer. *Nat. Commun.* **14**, 2757 (2023).
60. Das, S. et al. Nanoscale thickness octave-spanning coherent supercontinuum light generation. *Light Sci. Appl.* **14**, 41 (2025).
61. Kresse, G. & Furthmüller, J. Efficiency of ab-initio total energy calculations for metals and semiconductors using a plane-wave basis set. *Comput. Mater. Sci.* **6**, 15–50 (1996).
62. Perdew, J. P., Burke, K. & Ernzerhof, M. Generalized gradient approximation made simple. *Phys. Rev. Lett.* **77**, 3865–3868 (1996).
63. Grimme, S. Semiempirical GGA-type density functional constructed with a long-range dispersion correction. *J. Comput. Chem.* **27**, 1787–1799 (2006).
64. Hoover, W. G. Canonical dynamics: equilibrium phase-space distributions. *Phys. Rev. A* **31**, 1695–1697 (1985).